ORIGINAL RESEARCH

Biomimetic highly porous nanocellulose–nanohydroxyapatite scaffolds for bone tissue engineering

Jannika T. Korkeamäki · Ahmad Rashad · Kaia Berstad ·
Florian Weber · Kristin Syverud · Håvard Jostein Haugen ·
Kamal Mustafa

Abstract Wood-derived TEMPO-oxidized cellulose nanofibrils (CNFs) have potential as scaffolding for bone tissue engineering. Although biocompatible, the material lacks osteoconductive and appropriate mechanical properties. Incorporation of nanohydroxyapatite (nHA) and modification of scaffold preparation methods could improve applicability. In this study, freeze-dried porous scaffolds were prepared using a range of nHA (0, 20, 33, 50%) and CNF compositions. Not only the microarchitecture but also the chemical composition of the scaffolds was studied. Osteoblast-like osteosarcoma derived cells (Saos-2) were cultured on the scaffolds and their responses (viability, attachment, proliferation, and osteogenic phenotype) to the different scaffolds were documented. The results show that incorporation of nHA influenced the microarchitecture, mechanical stiffness and surface properties of the scaffolds. Moreover, biological characterization demonstrated good cell viability in all the groups. However, the increase of nHA concentration beyond 20% does not offer further advantages. It is concluded that the incorporation of 20% nHA resulted in the widest and most biomimetic pore size distribution, increased surface roughness and improved protein adsorption. These changes in material properties enhanced cell spreading and the osteogenic gene expression of osteoblast-like cells seeded on the scaffolds. Moreover, 20% nHA warrants further investigation as a potential scaffolding material for bone tissue engineering.

J. T. Korkeamäki · A. Rashad (✉) · K. Berstad ·
K. Mustafa (✉)
Center of Translational Oral Research (TOR), Department
of Clinical Dentistry, University of Bergen, 5009 Bergen,
Norway
e-mail: Ahmad.Rashad@uib.no

K. Mustafa
e-mail: Kamal.Mustafa@uib.no

F. Weber · H. J. Haugen
Department of Biomaterials, Institute of Clinical Dentistry,
University of Oslo, 0317 Oslo, Norway

K. Syverud
RISE PFI, 7491 Trondheim, Norway

K. Syverud
Department of Chemical Engineering, Norwegian
University of Science and Technology (NTNU),
7491 Trondheim, Norway

Graphical abstract
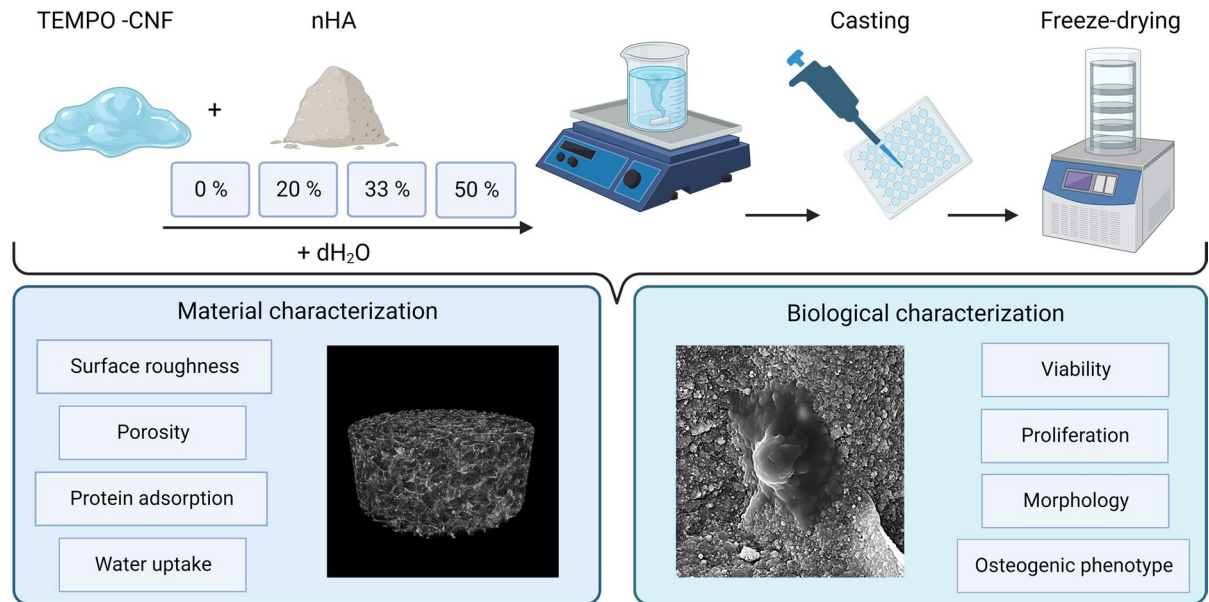
Created with BioRender.com

Introduction

Functional bone implants are increasingly used in a wide range of surgical procedures, in trauma surgery, treatment of tumors, tooth loss and osteoporosis. Increasing life expectancy will lead to even greater demand for such procedures (Bharadwaz and Jayasuriya 2020). There is also an urgent need to develop efficient alternative treatment options to autografts and allografts, circumventing the inherent disadvantages of limited availability of tissue and innate immune responses.

Bone is a unique organ with the capacity to self-repair and regenerate. However, some conditions present barriers to adequate self-healing, such as large bone defects, pathological conditions, or infection (Tang et al. 2016). Bones act as scaffolding for the body and are composed of two distinct forms of tissues: one is porous and the other dense. The porous bone (cancellous or trabecular bone) is a sponge-like tissue with pore sizes in the range of 100–500 μm. Scaffolds developed for bone tissue engineering should be capable of replicating the natural porosity of the bone to support cell/tissue growth (Oryan et al. 2014; Thavornyutikarn et al. 2014). Bone tissue comprises a small fraction of cells, surrounded by extensive amounts of extracellular matrix (ECM). The ECM is a biocomposite of nanohydroxyapatite (nHA; $Ca_{10}(PO_4)_6(OH)_2$), the major component of the mineral deposit and collagen, the most abundant organic component (Allori et al. 2008).

In analogy with collagen, cellulose is one of the world's most abundant natural and renewable materials and the main building block of trees and other plants. In plants, cells are surrounded by an ECM in the form of a thick cell wall, composed of a network of cellulose nanofibrils embedded in a highly cross-linked matrix of polysaccharides (Cosgrove 2005). Cellulose is a polysaccharide biopolymer, free of animal and microbial origins. Because of its

nanostructure, biocompatibility, low cost and availability, it can replace collagen (Lin and Dufresne 2014). Wood-based cellulose nanofibrils (CNFs) can be extracted stepwise from plants. Initially, a pulping process removes lignin and liberates the cellulose pulp fibres, which can be further oxidized using 2,2,6,6,-tetramethylpiperidine-1-oxyl radical (TEMPO), followed by mechanical treatment, reducing the larger sized diameter of (μm) wood pulp cellulose to smaller (nm) fibrils. (Lin and Dufresne 2014; Saito et al. 2006) As a result of the TEMPO-mediated oxidization isolation, CNFs are usually available in the form of gel-like materials (Masruchin et al. 2015). Our previous work with TEMPO-oxidized CNF hydrogels demonstrate suitable cell spreading and phenotypical morphology of fibroblasts (Rashad et al. 2017). However, all hydrogels, including CNFs, have poor mechanical properties and cannot stimulate bone-forming cells to form a mineralized matrix (Xavier et al. 2015).

Although a wide range of biopolymers and nHA scaffolds has been used for bone tissue engineering (Bharadwaz and Jayasuriya 2020), including the nanocomposites of cellulose and nHA (Ao et al. 2017; Daugela et al. 2018; Feroz and Dias 2021; He et al. 2018; Hokmabad et al. 2019; Palaveniene et al. 2019; Sofi et al. 2021), the osteogenic properties of these scaffolds have not been thoroughly documented. In many of these studies cellulose was used merely as the filler component of another scaffolding material, such as polycaprolactone, chitosan or collagen. Moreover, the effect of different nHA concentrations on the physicochemical properties of CNFs is not well documented.

To address these issues, the aim of this study was to prepare and characterize biomimetic porous nanostructured scaffolds for bone tissue engineering, by incorporating TEMPO-oxidized CNF hydrogels with different concentrations of nHA, an inorganic ceramic phase, to mimic closely the physiochemical nature of bone. We hypothesized that the addition of nanohydroxyapatite particles could act as nucleation sites for mineralization, thus improving the mechanical properties of the hydrogels, and affecting the porosity and pore sizes of the formed scaffolds. Freeze–dried scaffolds were prepared and evaluated for chemical composition, roughness, porosity, mechanical stiffness, swelling and protein adsorption. In addition, an osteoblast-like osteosarcoma-derived cell line (Saos-2)

was used to evaluate the seeding efficiency, viability, proliferation, and osteoblast-like phenotype of cells seeded on the scaffolds.

Materials and methods

Preparation of CNF gel-like material

TEMPO-mediated oxidized nanocellulose gel was produced by chemical and mechanical treatment of fully bleached, never-dried softwood kraft pulp, kindly donated by Södra Cell (Växjö, Sweden), as reported previously (Rashad et al. 2017). Briefly, wood pulp was immersed in water containing 2,2,6,6-tetramethylpiperidinyl-1-oxyl (TEMPO; Sigma-Aldrich, St. Louis, MO, USA) and sodium bromide. Then 2.5 mmol NaClO/g dry cellulose was slowly added to the slurry, at a constant pH of 10.5. One hour later, the pH was adjusted to 7 and methanol was added to quench the oxidation. Finally, the cellulose was washed thoroughly until the conductivity of the filtrate was below 5 μS/cm. The oxidized fibres were fibrillated using a Rannie 15 type 12.56X homogenizer (APV, SPX Flow Technology). The content of carboxyl and aldehyde groups introduced to the surface of the fibers was quantified by electric conductivity titration. The prepared samples had a solid content of $1.06 \pm 0.01\%$ and aldehyde and carboxyl groups of 211 ± 60 μmol/g and 764 ± 60 μmol/g, respectively (Rashad et al. 2017).

Preparation of cellulose nano-hydroxyapatite gel and scaffolds

TEMPO-oxidized cellulose nanofibril (CNF) gel stock (1% solid content, RISE PFI, Trondheim, Norway) was stirred for 15 min to achieve a homogenous suspension. Hydroxyapatite nanopowder (nHA; <200 nm, Sigma Aldrich, St. Louis, MO, USA) was weighed to reach final concentrations of 50%, 33%, 20% and 0% w/w, mixed with distilled water, and stirred for 15 min. CNFs and nHA suspensions were then combined and stirred for 15 min to achieve a homogenous gel. The gel was cast in 48-well plates and leveled on a shaker for 10 min. The casts were frozen at −20 °C for 24 h and then transferred to a

freeze–dryer for 48 h. The final scaffolds were cut into 2–3 mm-thick slices for further analysis.

Scanning electron microscopy and energy dispersive x-ray (EDX)

To study the surface morphology and to evaluate the Ca-P ratio, samples were analyzed by scanning electron microscopy (SEM) (Hitachi Analytical TableTop SEM TM3030, Hitachi, Tokyo, Japan) at 15 keV. The samples were gold sputtered (Sputter Coater 108 auto, Ted Pella INC. California, USA) before observation at two different magnifications (100× and 1000×). Elemental distribution analysis was undertaken by energy-dispersive X-ray spectroscopy (EDX), with the aforementioned apparatus. Elemental composition was recorded, and average values were calculated from 3 different randomly selected areas.

Fourier transform infrared spectrometry (FTIR)

Attenuated total reflection Fourier transform infrared spectrometry (ATR-FTIR; Spectrum One, Stamford, CT, USA; PerkinElmer, Waltham, MA, USA) was used to analyze chemical structures. Spectra were recorded at 2 cm^{-1} resolution with an average of 64 scans from 4000–650 cm^{-1}. Three measurements per group were taken ($n = 3$). Spectral data analysis, baseline correction, normalization, and band area were recorded using Perkin Elmer Applications Spectrum software.

Atomic force microscopy (AFM)

The topography of nHA/CNFs scaffolds was analyzed with an atomic force microscope (MFP 3D; Asylum Research, Santa Barbara, CA, USA). The surfaces were scanned in contact mode with the scan direction perpendicular to the cantilever (probes: OMCL-AC240TS, Olympus Optical Co. Ltd., Tokyo, Japan). Height profiles were extracted after leveling and removing scanning artifacts using Gwyddion.

Micro-computed tomography (μCT)

For micro-computed tomography (μCT), freeze–dried samples were scanned at 9 μm resolution, 40 kV and 228 μA using the SkyScan 1172 μCT imaging system (SkyScanVR v.1.5.23, Kontich, Belgium). Both

the ROI and VOI were kept constant for each analysis group. 2D images were captured every 4° through 360° rotation and then reconstructed by Skyscan NRecon software, as reported previously (Ojansivu et al. 2019). Three replicas were used.

Mechanical testing

Young's Modulus ($n = 6$) was used to calculate tensile strength, using a universal tensile testing machine (MTS, 858 Mini Bionix II instrument, Eden Prairie, MN, USA) at room temperature and a tensile displacement rate of 0.1 mm s^{-1}.

Swelling

Freeze dried samples ($n = 5$) were weighed and immersed in water for 30 min, 1, 2, 4, 8, 24 and 48 h. At each timepoint, the samples were removed from the water and excess water was removed. The samples were then weighed. Dry weight, w_0, of the scaffolds was used to calculate the weight increase in water uptake, where w_t represents the weight of a swollen scaffold at the timepoint.

$$Swelling\,(\%) = \frac{w_t - w_0}{w_0} \times 100$$

Protein adsorption

Cut samples ($n = 5$) were autoclaved and soaked for 24 h in 1 ml of 15% fetal bovine serum (Sigma-Aldrich) in McCoy's 5 A (ATCC, Manassas, VA, USA). The samples were incubated at 37 °C and 5% CO_2, then washed with Dulbecco's phosphate-buffered saline (DPBS; Gibco, Thermo Fisher Scientific, Waltham, MA, USA), immersed in 1 ml of 2% sodium dodecyl sulfate (Sigma Aldrich, St. Louis, MO, USA) and incubated overnight at room temperature. To measure protein adsorption, a Pierce™ BCA Protein Assay Kit (Thermo Fisher Scientific) was used as per the manufacturer's instructions. The absorbance was read at 562 nm, using a multimode microplate reader (Varioskan™ LUX, VLBL00D0, Thermo Fisher Scientific).

Biological characterization

Osteoblast-like cells derived from a human osteosarcoma cell line (Saos-2 cells) were obtained from ATCC (Manassas, VA, USA) and maintained as well as expanded in McCoy's 5 A medium, supplemented with 1% penicillin-streptomycin (P/S; Thermo Fisher Scientific, Gibco™, 10 000 U/mL) and 15% FBS (GM). To investigate the biological effects of the different scaffolds, 1×10^5 Saos-2 cells were seeded on top of autoclaved and medium pre-soaked scaffolds. To study the osteogenic potential of the different nHA concentrations, scaffolds were cultured in osteogenic medium (OM) (GM + L-ascorbic acid 173 µM; dexamethasone 10 nM; β-glycerophosphate 10 mM, Sigma Aldrich).

After seeding, the cells were allowed to attach for 4 h and the scaffolds were transferred to new wells. The cells attached to the bottom of the wells (unattached to the scaffold) were quantified using AlamarBlue assay (AlamarBlue HS, Invitrogen—Thermo Fisher Scientific) as per the manufacturer's instructions. Three replicas from each group were incubated at 37 °C while protected from direct light. Controls for background (containing OM only), and 100% efficiency (2D culture) were used. The fluorescence (excitation at 540 nm, emission at 570 nm) was read with a microplate reader. The seeding efficiency was calculated as follows.

$$Seeding\ efficiency(\%) = \frac{(Seeded\ cells - escaped\ cells)}{Seeded\ cells} \times 100$$

The viability of Saos-2 cells was evaluated using a Live/Dead (L/D) Viability/Cytotoxicity Kit for mammalian cells (Invitrogen, Thermo Fisher Scientific). After washing with DPBS, a solution of DPBS containing Calcein AM (667 nM) and Ethidium homodimer-1 (333 nM) was added to cover the scaffolds. The samples were incubated in the dark for 40 min at RT. The samples were then washed with DPBS and imaged under a fluorescent microscope (Nikon Eclipse Ti, Tokyo, Japan). The viability of the cells was assessed on days 1, 7, 14 and 21.

The proliferation profile of Saos-2 cells was studied on days 1, 4, 7 and 14 ($n=6$). Scaffolds were collected, washed with DPBS, frozen at − 80 °C in a lysate solution (0.1% Triton X-100, 300µL), and thawed twice. The samples were then sonicated (30 s on ice) and vortexed. Finally, 20 µL were pipetted from the supernatant and added to 180 µL of the Quant-iT PicoGreen dsDNA Reagent (Invitrogen—Thermo Fisher Scientific) working solution, as per the manufacturer's instructions. The results were read with a microplate reader at 485/535 nm.

To examine the morphology of both the scaffold surface and the Saos-2 cells on the scaffolds, samples were collected on days 1 and 7 and washed twice with DPBS. The scaffolds were fixed for 30 min with 3% glutaraldehyde 0.02 M Na-cacodylic buffer with sucrose, washed twice for 5 min with 0.1 M Na-cacodylic buffer with sucrose and once with 1:1 diluent with distilled water. The samples were then dehydrated to 100% ethanol in 5 min cycles and left to air dry. Next, the samples were sputter-coated with a 100 Å layer of gold and imaged in a scanning electron microscope (SEM) (Phenom XL Desktop, Thermo Fisher Scientific).

Osteogenic potential of the seeded cells

After osteogenic induction, the alkaline phosphatase (ALP) activity of the seeded cells was determined on days 1, 7 and 14 ($n=6$). Scaffolds were collected, washed with DPBS, frozen at − 80 °C in lysate solution (0.1% Triton X-100, 300µL) and thawed twice. To assess the results, a 1:1 ratio of the sample and p-Nitrophenyl Phosphate Liquid Substrate System (Sigma Aldrich) was transferred to 96-wells and incubated for 15 min at 37 °C. A solution of 1.0 M NaOH was added to each sample to stop the reaction before measuring the absorbance at 405 nm. Finally, the ALP activity was normalized to the DNA content in each scaffold.

To investigate osteogenic gene expression, samples ($n=6$) were collected on days 7 and 21, washed with DPBS and frozen to − 80 °C before RNA extraction. The samples were then thawed and processed with a Maxwell RSC simplyRNA Cells Kit (Promega, Madison, WI, USA) according to the manufacturer's instructions. The RNA concentration and quality were measured with a spectrophotometer (Nanodrop ND-1000, Nanodrop Technologies, Wilmington, DE, USA). Complementary DNA was then synthesized with High-Capacity cDNA Reverse Transcription Kit (Applied Biosystems Thermo Fisher Scientific, Waltham, MA, US). Finally, the quantitative real-time polymerase chain reaction (qRT-PCR) was

determined with the StepOne™ RT-PCR System (Applied Biosystems), using the TaqMan Fast program (×40: 95 °C, 1 s – 60 °C, 20 s), and the TaqMan Fast Universal PCR Master Mix (Applied Biosystems). The following genes were chosen as indicators of osteogenic commitment: runt-related transcription factor 2 (RUNX2, Hs01047973_m1), alkaline phosphatase (ALP, Hs01029144_m1), collagen type I (COLI; COLIA2, Hs01028956_m1), osteopontin (OP; SPP1, Hs00960942_m1) and osteocalcin (OCN; BGLAP, Hs01587814_g1) (Thermo Fisher Scientific). Glyceraldehyde-3-phosphate dehydrogenase (GAPDH; Hs02758991_g1Thermo Fisher Scientific) served as an endogenous control. The $2^{(-\Delta\Delta Ct)}$ method was used to determine relative quantification of gene expression. Gene expression levels were calculated by comparison with GAPDH and normalized to the expression level in the control group (0%) on day 7. The mean $\Delta\Delta Ct$ values were subjected to statistical analysis (Livak and Schmittgen 2001).

Statistical analysis

Chemical composition, µCT, swelling and protein adsorption data are represented as mean ± SD. For mechanical testing, seeding efficiency, proliferation, normalized ALP activity and gene expression, statistical analysis was undertaken using IBM SPSS Statistics (Version 28.0.1.1) and Prism software (GraphPad software, San Diego, CA, USA). One-way ANOVA with Tukey was used to test significance among the four groups. Paired student's T-test was used to test significance between timepoints. The differences were considered statistically significant at $p < 0.05$.

Results and discussion

Scaffold preparation

The mixed gel casts used in scaffold preparation are presented in Fig. 1a. Here the increase in nano-hydroxyapatite (nHA) concentration can be seen as an increased opacity in the casts. The gels are visibly even and are considered successful homogenous mixtures. The freeze–dried samples are presented in Fig. 1b. After freeze–drying the samples were visibly similar to one another.
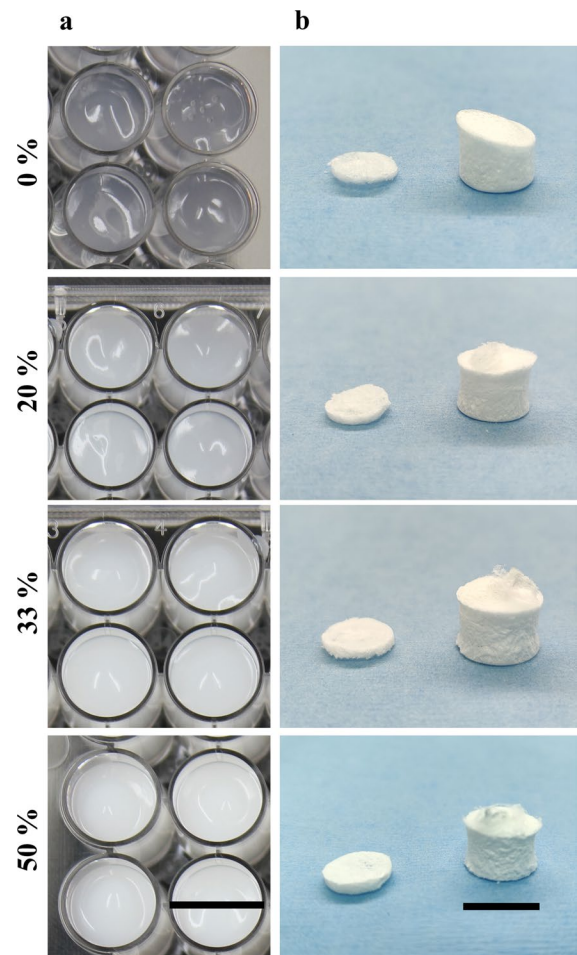

Fig. 1 Sample preparation from mixed gel (**a**), to freeze–dried and cut scaffolds (**b**). Scale bar 12 mm

Differences in scaffold composition

Energy dispersive X-ray analysis (EDX) was used to confirm the elemental composition of the samples in terms of calcium (Ca) and phosphorous (P). As shown in Fig. 2a, the results confirm the successful mixing and a clear difference among the groups, reflecting the lack of Ca and P in the pure cellulose nanofibril (CNF) scaffolds.

FTIR was used to investigate the interaction between CNFs and nHA (Fig. 2b). The CNF samples had distinct peaks at 1604, 1420, 1370, 1320, 1160, 1057, 1033 and 668 cm^{-1}. The peaks at 1604 and 1420 cm^{-1} are related to the stretching of the carboxylate group (Rashad et al. 2017, Masruchin et al. 2015, Soni et al. 2015), whereas the 1370 shows C–H

a

b
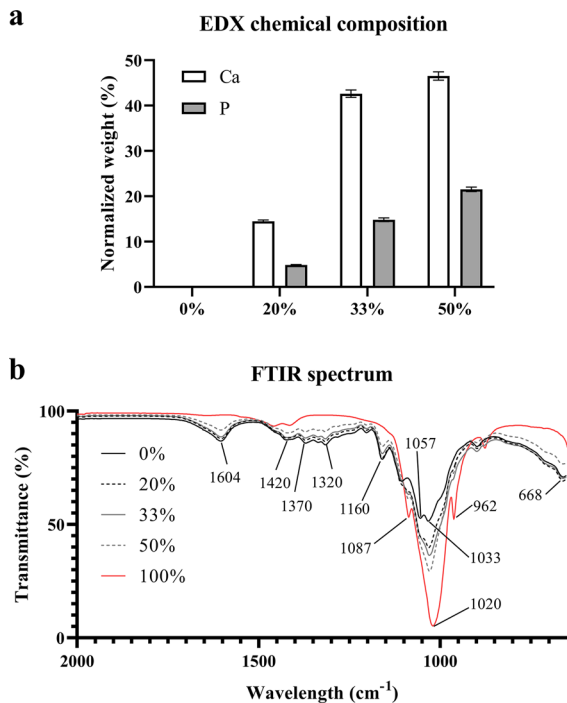
Fig. 2 **a** EDX analysis of chemical composition showing calcium (Ca) and phosphorous (P), normalized to weight ($n = 3$). **b** FTIR-spectrum of nHA (0–100%) and CNF composition ($n = 3$)

bending (Soni et al. 2015). Moreover, the C–O–C asymmetric stretching vibration at the β-glycosidic linkage, which was connected to the cellulose chain, was identified as the source of the peak at 1160 cm^{-1} (Palaveniene et al. 2019). The peaks at 1320, 1057 and 1033 cm^{-1} were related to C–O stretching (Daugela et al. 2018; Masruchin et al. 2015). The results also show the C–OH bending at 668 cm^{-1} (El Idrissi et al. 2022).

The pure nHA (Figs. 2b and 100%) had distinct peaks at 1087, 1020 and 962 cm^{-1}, which were attributed to the stretching vibration of P–O of the PO_4^{3-} group (Daugela et al. 2018; Palaveniene et al. 2019). At these peaks the absorption increased with increasing nHA incorporation. In addition, the domination of nHA in relation to CNFs can be seen in the shift of the most substantial peak of the CNFs (1033 cm^{-1}) towards the strongest peak in nHA (1020 cm^{-1}).

In addition to the EDX and FTIR analysis, the increase in nHA concentration is visible in the images from the scanning electron microscope (SEM) and atomic force microscopy (AFM) (Fig. 3a, b). CNFs alone (0%) present a very smooth surface in the SEM image, but when the nHA is incorporated, the increase in surface roughness is discernible as white specks on the CNF backbone. In the AFM images, the size variation in the CNFs is also visible. Although thin (nanoscale) in nature, the length of the fibres varies hugely (nano-microscale), as also shown previously (Rashad et al. 2018). Although the relatively even distribution of nHA particles is visible in both SEM and AFM images, agglomerates of CNFs and nHA can be discerned. The 0% nHA samples had a surface roughness of around 700 nm, whereas the surface roughness of the 50%, 33% and 20% samples was over 1 μm.

Scaffold microarchitecture changed with material composition

The micro-computed tomography (μCT) results illustrate the presence of nHA (Fig. 4a) and its effects on scaffold microarchitecture (Fig. 4b–d). In accordance with the EDX, in the μCT the scaffolds become more radiopaque with increasing nHA content, as calcium absorbs the x-rays efficiently. While the scaffold with 50% nHA showed the highest density, the pure nanocellulose scaffold was radiolucent.

All four groups presented a high total porosity (73.9–93%) and reached 100% interconnectivity. The highest total porosity was achieved with CNFs alone (93% ± 3.59, Fig. 4b), whereas the highest object surface area (2104.03 mm^2 ± 84.22) was seen with the 50% nHA. This is directly related to the amount of dry matter in the scaffold, as the specific surface (surface/object volume ratio) decreases with nHA addition. In the literature, the importance of total porosity, describing the percentage volume of void in a scaffold, is frequently mentioned (Karageorgiou and Kaplan 2005). However, in some studies, values as low as 50% are reported (Entezari et al. 2019; Ratheesh et al. 2021) while others are higher at 70–90% (Mygind et al. 2007; Whang et al. 1999; Sicchieri et al. 2012). It should be noted that this parameter is rarely compared in the experimental set-up, although its relationship to, for example, mechanical stiffness is widely accepted. The scaffolds in the current study exhibit high total porosity and interconnectivity, the flow of fluids through interconnected pores. In other words, the scaffolds provide large, connected surface

Fig. 3 **a** SEM scan of the different groups, scale bar 50 μm ($n = 3$). **b** AFM images of the CNF-nHA groups, scale bar 30 μm
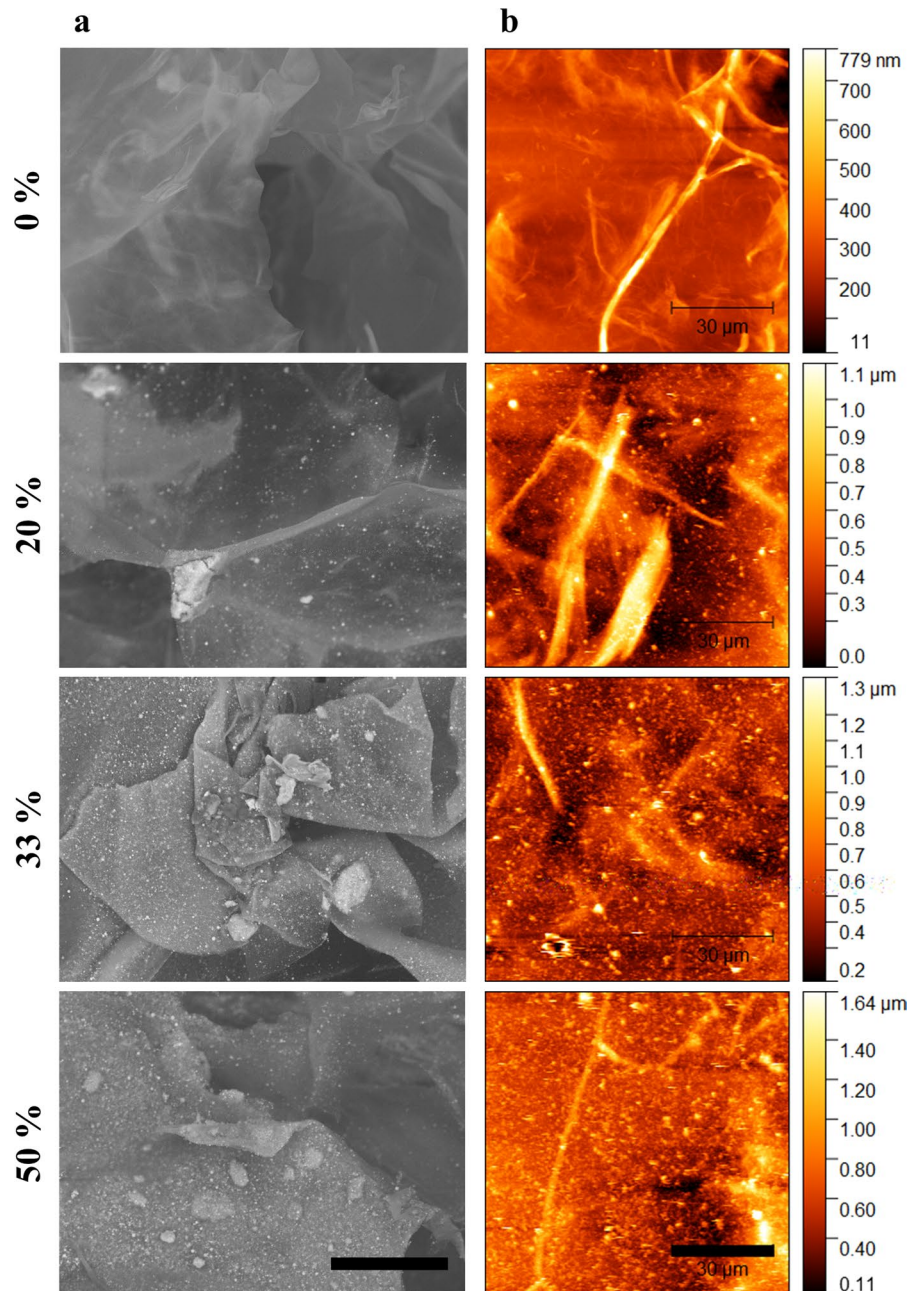
areas, facilitating cell seeding, migration, and nutrient and oxygen flow throughout the structures (Bobbert and Zadpoor 2017; Entezari et al. 2019).

As expected, mechanical stiffness (Fig. 4c) followed the trend of total porosity. The samples with highest porosity (0% nHA) had the lowest modulus (0.188 MPa ± 0.041). The 50% nHA samples had significantly higher mechanical stiffness than all

other groups (0.601 MPa ± 0.155). Young's modulus for trabecular bone is 0.05–0.5 GPa, a 10^3-fold difference from the mechanical stiffness recorded in the current study (Hutmacher et al. 2007). However, compared to previous work on the hydrogel nature of CNFs, Young's modulus increased 10^2-fold after freeze–drying (Syverud et al. 2014). In addition, the

mechanical stiffness increased significantly with nHA incorporation above 33%.

Pore size, expressed as the diameter of a single unit of void, is closely associated with porosity, but sets the scale of the environment that cells sense in a scaffold (Bobbert and Zadpoor 2017; Huri et al. 2014). In the current study, 20% nHA resulted in the widest range of pore size distribution (9–422 μm). However, with increasing nHA, the pore size became smaller, and the distribution became narrower. Consequently, the 50% nHA had the smallest pore size and distribution (9 − < 206 μm, Fig. 4d). The pre-freezing temperature of −20 °C used in scaffold preparation affects the median pore size achieved (Petrauskaite et al. 2016; Haugh et al. 2010; Murphy et al. 2010). Compared to lower temperatures (and therefore, faster freezing), such as −80 °C, the chosen temperature enables the expansion of water (Petrauskaite et al. 2016). As a result, the nucleation and the formation of ice crystals is larger in size, directly affecting the size of formed pores (Haugh et al. 2010). The decrease in pore size associated with incorporation of nHA is commonly reported in studies on freeze–dried scaffolds (Hokmabad et al. 2019; Kim et al. 2005; Palaveniene et al. 2019). On the other hand, the greater pore size distribution of the 20% nHA in the current study indicates a CNF-nHA ratio-specific interaction, enabling enlarged nucleation and ice crystal formation during the pre-freezing step. It could be speculated that the same does not occur at higher nHA concentrations because of higher dry matter content in the composition of the scaffolding.

Swelling and protein adsorption

The swelling and protein adsorption data are presented in Fig. 5. All groups demonstrated high water uptake: the highest was in the 0% nHA after 48 h incubation (5983 ± 454%). Water uptake decreased with further nHA incorporation, with the lowest swelling in the 50% nHA after 48 h (3472 ± 293%) (Fig. 5a). The decrease in swelling can be attributed to the decreasing total porosity associated with incorporation of nHA (Fig. 4b).

A similar trend was observed for protein adsorption. The 0% nHA samples could adsorb the highest amount of proteins per object surface area (0.379 ± 0.086 μg/mm^2) provided by FBS (Fig. 5b). The 20% nHA showed similar results

(0.361 ± 0.089 μg/mm^2), whereas the samples with higher concentrations of nHA did not perform as well (33%: 0.288 ± 0.034 μg/mm^2; 50%: 0.276 ± 0.018 μg/mm^2). These results are of interest because the CNF scaffold alone had a smoother surface topography (Fig. 3a and b – 0%) and one of the smallest surface areas (Fig. 4b). However, 0% nHA had the highest specific surface and could present more favourable surface chemistry, such as carboxyl groups (McClary et al. 2000).

Seeding efficiency, viability, and proliferation of Saos-2 cells

The viability, seeding efficiency and proliferation are presented in Fig. 6. In all groups, seeding efficiency (Fig. 6a) was relatively low, ranging from 40 to 60%. This could be due to the highly porous and interconnected structure, leading to cells flowing through the scaffold by gravity before adherence. The highest initial cell numbers were recorded for 20% nHA (57.82 ± 7.71%).

Even with the variation in initial cell numbers, there is little difference in relative proliferation on day 1 (Fig. 6b). However, from day 7 even significant differences can be seen, where 0% nHA outperforms 50% nHA. The highest relative cell proliferation occurs on day 14 (20% nHA), which is significantly higher than all the other groups. In addition, all groups presented high cell viability (Fig. 6c) over 4 days, indicating an initial nontoxic effect of the scaffolds.

The differences in seeding efficiency and proliferation are closely related to the material and surface properties. Both swelling and protein adsorption are desirable biological responses. Swelling, or water uptake, aids cell seeding, nutrient uptake, ion flow and waste exchange, both in vitro and in vivo. Protein adsorption can make the scaffolding a preferred site, attractive for cells such as osteoblasts to adhere and spread (Wilson et al. 2005). Yang et al. (2013) described the mechanism of cells interacting with materials with the concept of "protein adsorption—cell behaviour". It was shown that adhesion of cells is related to the presence of adsorbed proteins containing RGD-peptide motifs, to which cell surface integrins bind. Although manufacturers do not report the protein content of commercial FBS, the general ingredients and variation in content are reported in
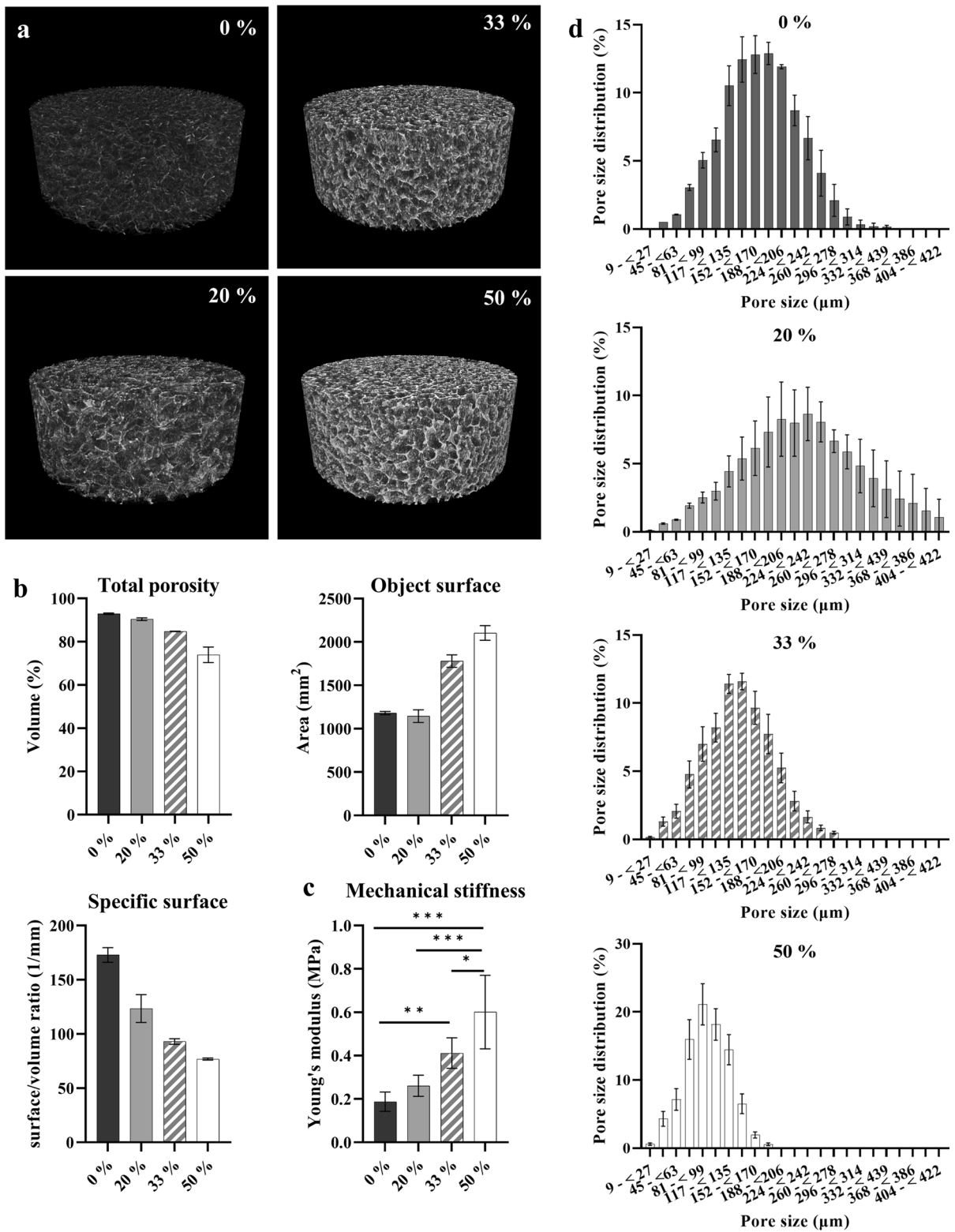
the literature (Lee et al. 2022). Of the over 90 proteins identified in FBS, fibronectin and vitronectin are those most frequently discussed with reference to cell adhesion and spreading (Hayman et al. 1985; Wilson et al. 2005). When this is related to the scaffold material in use, Webster et al. (2001) demonstrated increased adsorption of vitronectin to both calcium and nano phased alumina surfaces. This was corroborated by Kilpadi et al. (2001), reporting increased fibronectin and vitronectin adsorption to hydroxyapatite compared to commercial metals used as hard-tissue materials. Therefore, although the quantity of adsorbed protein might be greater in the 0% scaffold surface, the quality might be better in nHA-incorporated scaffolds, because of the material properties.

The 20% nHA demonstrates more effective cell attachment and proliferation, most likely due to the largest pore size distribution (Fig. 4d), high water uptake (Fig. 5a) and theoretically higher preferable protein adsorption qualities. Murphy et al. (2010) suggested that a smaller pore size (85–120 µm) would decrease cell filtration and migration, limiting cells to aggregate more on the outer perimeters of a scaffold. This could explain the lowest proliferation on 50% nHA.

It was of interest to note that despite high porosity, high specific surface area, water uptake and protein adsorption, the 0% nHA scaffold did not demonstrate superior results. Therefore, it could be argued, that incorporating nHA into the scaffolds offers advantages through increased surface roughness (Deligianni et al. 2001) and the aforementioned beneficial protein adsorption.

Differences in cell morphology disclosed by SEM

SEM images of cell-cultured samples are presented in Fig. 7. All groups show attachment on day 1, with distinct cell bodies and nuclei. However, differences in cell morphology can be seen among the groups. In the 0% nHA samples, the cells are more spindle-like. In contrast, the cells attached on nHA samples are more polygonal on day 1. The differences become more distinct on day 7. On the 0% nHA, the cells maintain their spindle-like shapes whereas on the 20% nHA the cells are completely spread out over the scaffold surface in a sheet-like formation. A similar appearance can be noted on 33% nHA, with a decreasing trend on the 50% nHA, where the elliptical shape of the cell nuclei can still be discerned.

In accordance with the blank SEM and AFM results (Fig. 3a, b), the scaffolds with nHA exhibited greater surface roughness than the smooth surface of cellulose without nHA. It is of interest to note that the surface roughness can also be seen from the cell morphology, as the cells lie and anchor tightly on the nHA particles. Similar morphology and anchoring
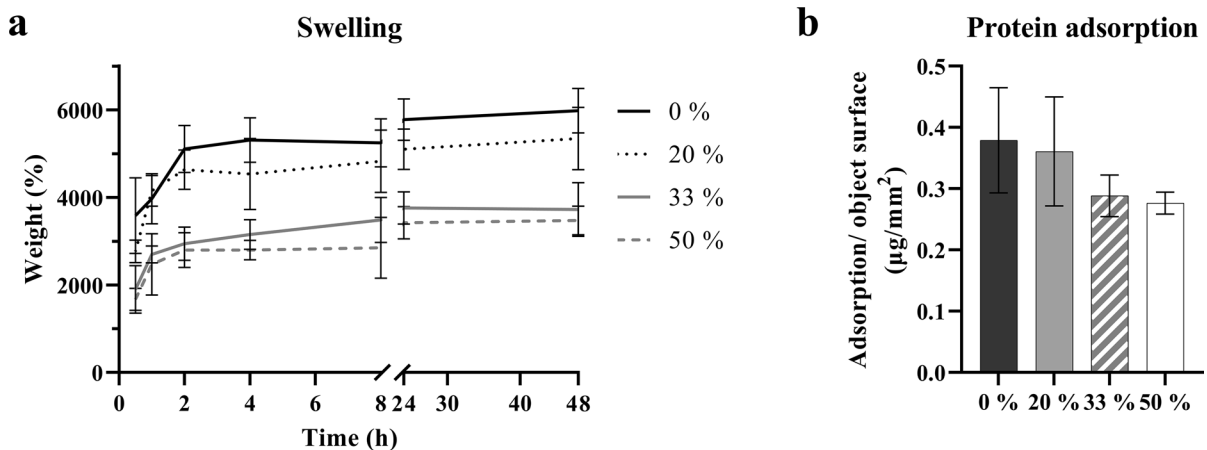

Fig. 5 **a** Swelling measured in dH$_2$O for 48 h ($n=5$). **b** Protein adsorption over surface area for 24 h ($n=5$)

Fig. 6 **a** Seeding efficiency measured after 4 h ($n = 3$). **b** Proliferation measured on days 1, 7 and 14. The results are presented relative to 0% group on day 1 ($n = 6$). Differences between groups are labeled as *$p < 0.05$, **$p < 0.01$, ***$p < 0.001$. **c** Viability of the cells on day 1 and day 4: live (cyanide), dead (magenta) and scaffold structure (grey). Scale bar 500 μm
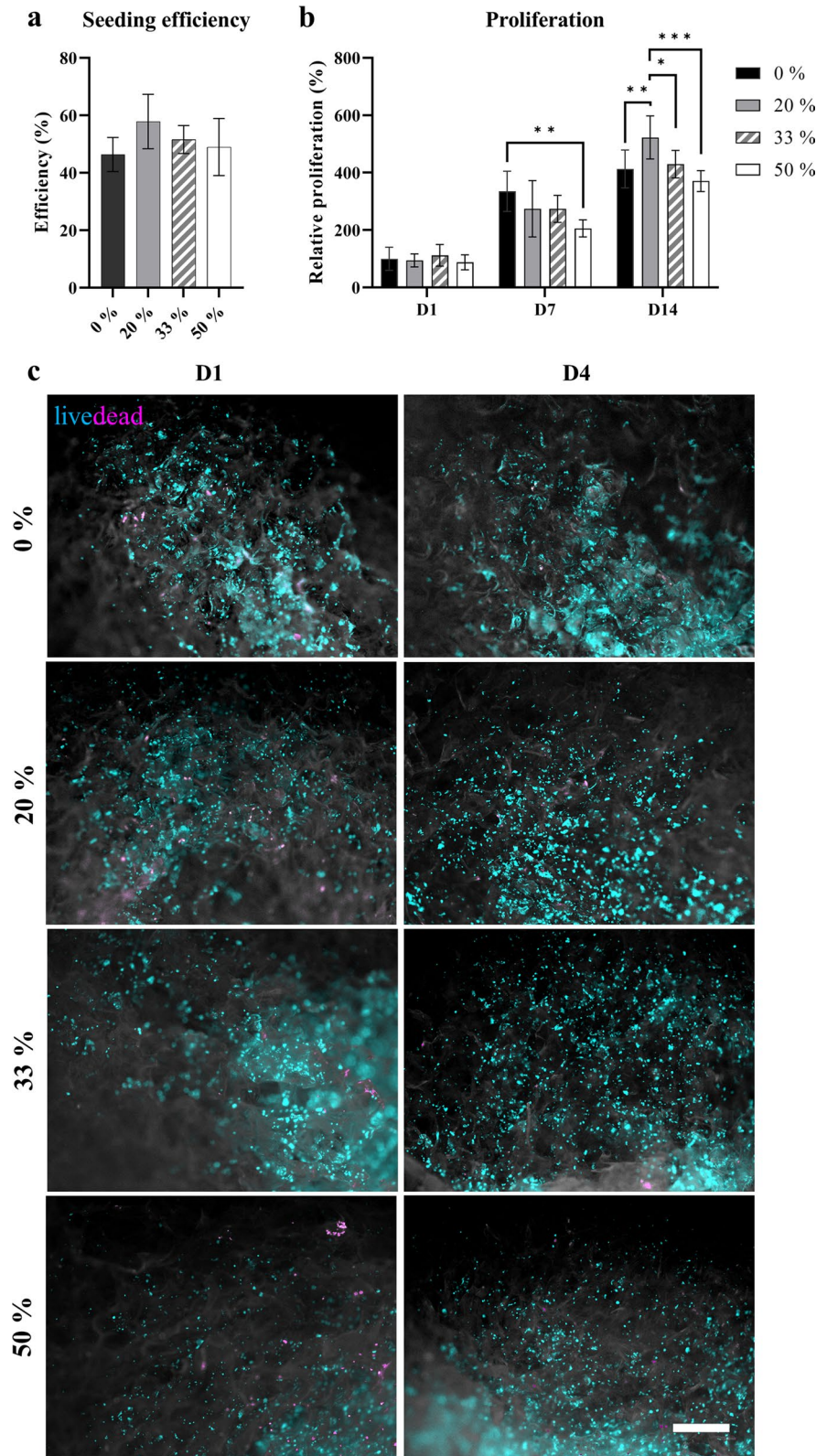
Fig. 7 SEM imaging of Saos-2 cells on top of the scaffolds on day 1 and day 7. Cells are indicated with white arrows. Scale bar 10 μm
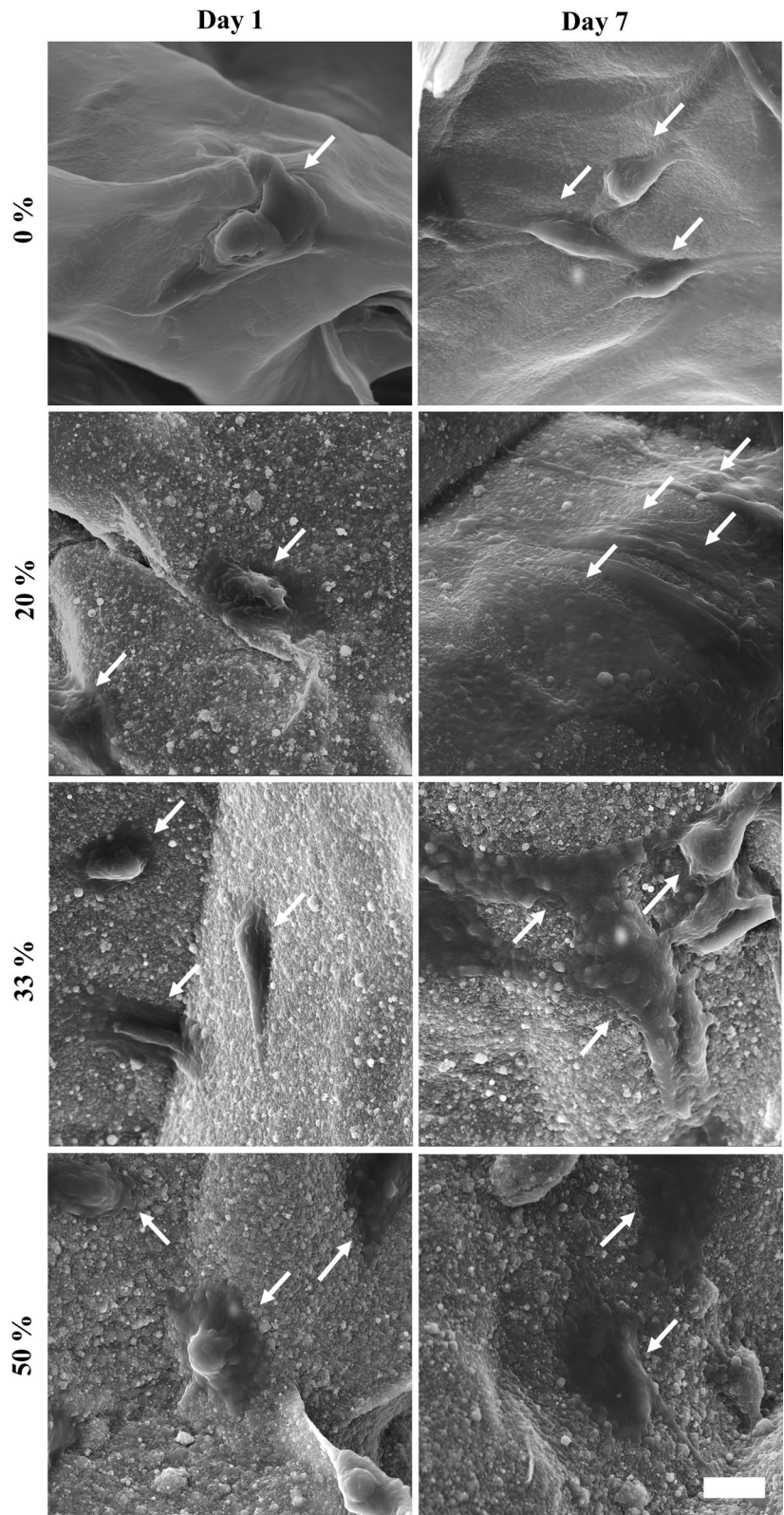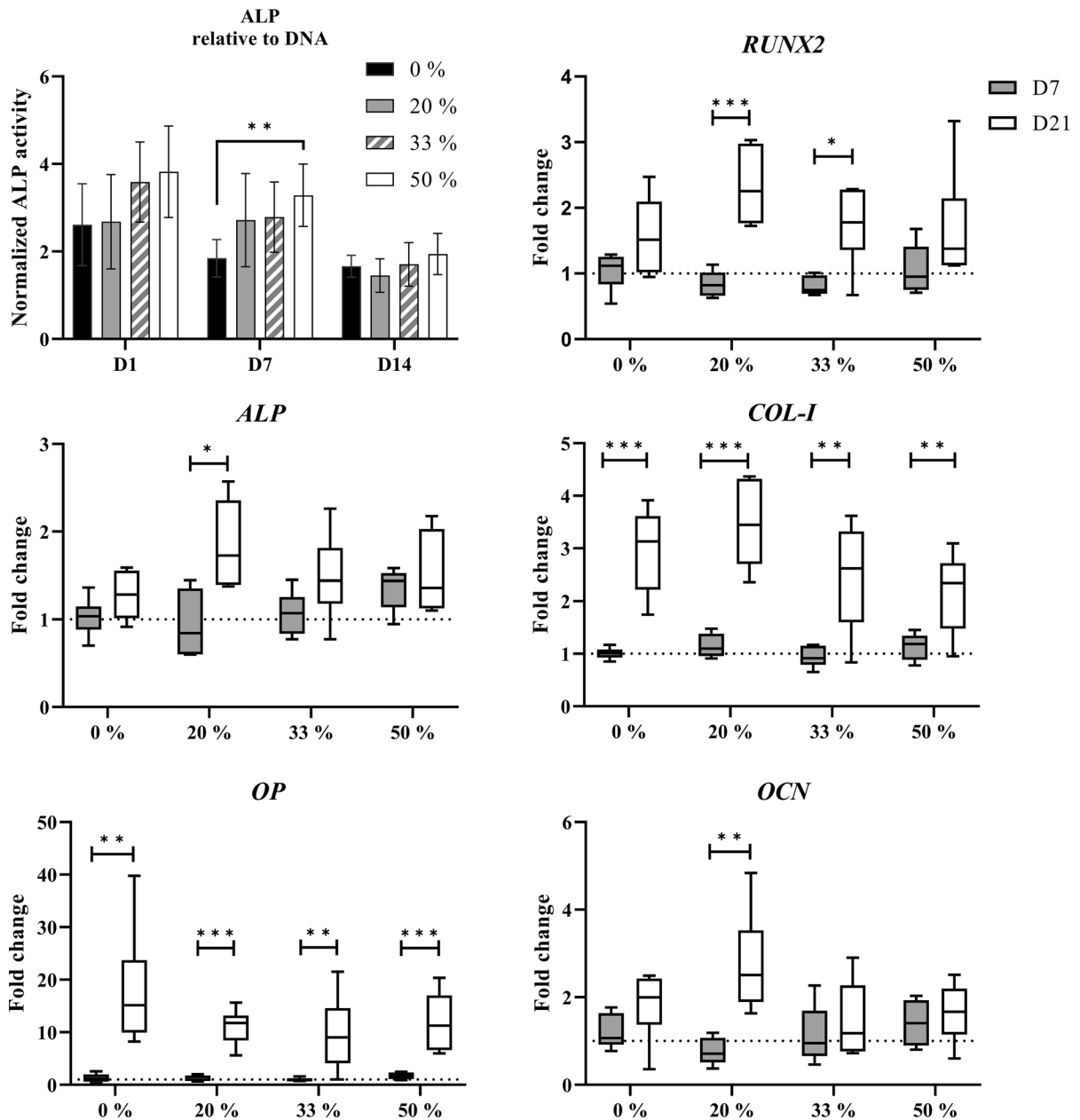
Fig. 8 Relative ALP activity on days 1, 7, and 14 is normalized to the amount of DNA ($n=6$). Differences between groups are labeled as $*p<0.05$, $**p<0.01$, $***p<0.001$. Expression of osteogenic genes: RUNX2, ALP, COL-I, OP and OCN on days 7 and 21, common legend. The results are relative to the D7 0% nHA samples ($n=6$). Differences between groups are non-significant. Differences between timepoints: $*p<0.05$, $**p<0.01$, $***p<0.001$

were reported by Daugela et al. (2018) with cellulose/nHA scaffolds. In all but the 0% nHA samples, the cells seem to continue to spread, from day 1 to day 7. Based on the SEM images, the cells seem to prefer the 20% nHA group over others, although similar cellular spreading can be observed in the 33% group. This is supported by comparing the mechanism of adhesion to smooth surfaces and a micron- or submicron scale environment. Zhu et al. (2004) demonstrated that a smooth surface prevents filopodia

formation, but filopodia scan the environment in numbers and when micro- or submicroscale cues are provided, they will mature into lamellopodia with enhanced cell attachment.

Moreover, Deligianni et al. (2001) studied different surface roughness properties on hydroxyapatite discs and concluded that increasing surface roughness enhanced cell adhesion and proliferation. Similarly, Hokmabad et al. (2019) studied ethyl cellulose-grafted-poly(ε-caprolactone) alginate nanofibrous scaffolds incorporated with nHA and recorded improved attachment and proliferation. Here it can be concluded that the nHA incorporation enhanced attachment and morphology of the cells through surface roughness.

Osteogenic phenotype expression

The normalized alkaline phosphatase (ALP) activity and osteogenic gene expressions are presented in Fig. 8. The ALP activity is at its highest level on day 1 in all the groups and decreases steadily to day 14. This could be explained by a longer expansion time before Saos-2 cells were seeded onto the scaffolds. The 50% nHA demonstrated the highest ALP activity on day 1 through the timepoints. However, the only significant difference among the groups could be found on day 7, between the 0% and the 50% nHA.

With reference to selected osteogenic markers, there were no significant inter-group differences. However, differences were detected between timepoints. For example, for the 20% nHA alone, *ALP* and *OCN* expression increased significantly from day 7 to day 21. Moreover, in both the 20% and 33% nHA groups, there were significant increases in expression of the early osteoblastic transcription factor *RUNX2* between the timepoints. Moreover, all groups exhibited significant increases in expression of *OP* and *COL-I* over time.

Bone formation is generally described as having three phases: proliferation, early differentiation with extracellular matrix maturation (ECM) and mineralization (Vimalraj et al. 2015; Huang et al. 2007). *Runx2*, an early osteogenic marker, is one of the most important transcription factors in the initial process of osteogenesis. Among the important effects, it activates other osteoblast differentiation marker genes, such as *ALP*, *COL-I*, *OP* and *OCN* (Vimalraj et al. 2015). When the differentiation process shifts from

proliferation to ECM maturation, *ALP* expression peaks in parallel with collagenous ECM formation (Lian and Stein 1995). *ALP* is a membrane-bound enzyme with an evident role in ECM mineralization, facilitating the calcification of collagen (Price et al. 2009; Murshed and McKee 2010). At this stage of osteogenic differentiation, however, the expression of both *ALP* and *COL-I* are required. In the last phase, in addition to the calcium phosphate mineral deposition, there is increased production of osteopontin and osteocalcin, proteins associated with the mineralized matrix (Beck and Knecht 2003; He et al. 2010). *OP* gene expression is also found at low levels in the early proliferative phase, whereas *OCN* is associated only with mineralization (Lian and Stein 1995).

When relating the gene expression results from the current study to the phases of osteogenic differentiation, only the 20% nHA follows through from beginning to end. Despite the significant increase in *Runx2* expression with the 33% nHA, it does not seem to be adequate to stimulate the process further into increased *OCN* expression. It could also be argued that the increase of *Runx2* expression is relatively late, but there are also reports of late *Runx2* expression in the mineralization phase (Lian and Stein 1995). However, when observing ALP activity and osteogenic gene expression, the type of cell used should be taken into account. Saos-2 cells are already osteoblast-like cells and should be evaluated for osteogenic phenotype rather than osteogenic differentiation. Therefore, we can accept earlier ALP activity, which might not correlate directly with *Runx2* and *ALP* expression (Czekanska et al. 2014). Of all gene expressions, the greatest fold change was recorded for *OP*. This correlates with a report that inorganic phosphate stimulates the expression of *OP* in osteoblasts (Beck and Knecht 2003). However, as there is also a significant increase with the 0% nHA, the increase is most likely stimulated by the osteogenic medium supplement, β-glycerophosphate, not the nHA in the scaffolds.

With reference to the osteogenic gene expression results of the current study, the achieved microarchitecture of the scaffolds should be considered. The reported ideal pore size for osteogenic activity and bone formation varies greatly in the literature, for both in vitro and in vivo studies. Mygind et al. (2007) suggested a preference for a smaller pore size of 200 µm in vitro and this was supported

by Brennan et al. (2019). However, contradictory results are reported by Huri et al. (2014) and Sicchieri et al. (2012) with preferred pore sizes of 1000–1500 μm and 850–1200 μm, respectively. The variation is not as pronounced in in vivo studies. While Tsuruga et al. (1997) and Whang et al. (1999) agreed on a pore size of 300–400 μm, two decades later Sicchieri et al. (2012) and Entezari et al. (2019) suggest ranges of 470–590 and 390–590 μm, respectively. However, a new approach to pore size range has recently been introduced: bimodal pore design, alternating smaller pores with larger ones to induce osteogenic differentiation in vitro and bone formation in vivo. In these more recent reports, there is closer agreement on pore sizes. In an in vivo study, Brennan et al. (2019) presented a bimodal design in which pore size alternated from 390 to 590 μm. In an in vitro study, Ratheesh et al. (2021) investigated pore sizes alternating from 100 to 530 μm. In the current study the biomimetic scaffolds have a range of pore sizes. The 50% nHA shows a narrower distribution, with the smaller pore size of 100 μm. However, on the 20% nHA scaffolding, pore size was more widely distributed, with both smaller (100–200 μm) and larger pores (350–400 μm), This material could be categorized as bimodal, although it presents a variety of pore sizes instead of two. The preferred pore size for osteogenic phenotype expression stated in the literature is in accordance with the gene expression results of 20% nHA in the current study.

Conclusions

Incorporating increasing amounts of nHA (0%, 20%, 33%, 50%) to CNF matrix modified the physical and biological properties of biomimetic freeze–dried scaffolds. While surface roughness, porosity, mechanical stiffness, swelling and protein adsorption correlate linearly with increasing nHA concentration, the pore size distribution did not follow the trend. In addition, the biological characterization revealed that nHA incorporation over 20% did not offer further advantages. The composite scaffolds supported cell proliferation and osteoblastic phenotype without cytotoxicity, with favourable responses to surface properties.

Inter-group comparison shows that 20% nHA seems to be superior in terms of favourable pore size

properties, observed cell morphology and osteogenic gene expression. The results imply that 20% nHA scaffolding has the greatest potential for further biomimetic bone tissue engineering investigations.

Declarations

Conflict of interest The authors declare no competing interests.

References

Allori AC, Sailon AM, Warren SM (2008) Biological basis of bone formation, remodeling, and repair-part II: extracellular matrix. Tissue Eng Part B Rev 14(3):275–283. https://doi.org/10.1089/ten.teb.2008.0083

Ao C, Niu Y, Zhang X, He X, Zhang W, Lu C (2017) Fabrication and characterization of electrospun cellulose/nano-hydroxyapatite nanofibers for bone tissue engineering. Int J Biol Macromol 97:568–573. https://doi.org/10.1016/j.ijbiomac.2016.12.091

Beck GR Jr, Knecht N (2003) Osteopontin regulation by inorganic phosphate is ERK1/2-, protein kinase C-, and proteasome-dependent. J Biol Chem 278(43):41921–41929. https://doi.org/10.1074/jbc.M304470200

Bharadwaz A, Jayasuriya AC (2020) Recent trends in the application of widely used natural and synthetic polymer nanocomposites in bone tissue regeneration. Mater Sci Eng C Mater Biol Appl 110:110698. https://doi.org/10.1016/j.msec.2020.110698

Bobbert FSL, Zadpoor AA (2017) Effects of bone substitute architecture and surface properties on cell response, angiogenesis, and structure of new bone. J Mater Chem B 5(31):6175–6192. https://doi.org/10.1039/c7tb00741h

Brennan CM, Eichholz KF, Hoey DA (2019) The effect of pore size within fibrous scaffolds fabricated using melt electrowriting on human bone marrow stem cell osteogenesis. Biomed Mater 14(6):065016. https://doi.org/10.1088/1748-605X/ab49f2

Cosgrove DJ (2005) Growth of the plant cell wall. Nat Rev Mol Cell Biol 6(11):850–861. https://doi.org/10.1038/nrm1746

Czekanska EM, Stoddart MJ, Ralphs JR, Richards RG, Hayes JS (2014) A phenotypic comparison of osteoblast cell lines versus human primary osteoblasts for biomaterials testing. J Biomed Mater Res A 102(8):2636–2643. https://doi.org/10.1002/jbm.a.34937

Daugela P, Pranskunas M, Juodzbalys G, Liesiene J, Baniukaitiene O, Afonso A, Gomes S (2018) Novel cellulose/hydroxyapatite scaffolds for bone tissue regeneration: in vitro and in vivo study. J Tissue Eng Regen Med 12(5):1195–1208. https://doi.org/10.1002/term.2651

Deligianni DD, Katsala ND, Koutsoukos PG, Missirlis YF (2001) Effect of surface roughness of hydroxyapatite on human bone marrow cell adhesion, proliferation, differentiation and detachment strength. Biomaterials 22(1):87–96. https://doi.org/10.1016/s0142-9612(00)00174-5

El Idrissi N, Belachemi L, Merle N, Zinck P, Kaddami H (2022) Comprehensive preparation and catalytic activities of Co/TEMPO-cellulose nanocomposites: a promising green catalyst. Carbohydr Polym 295:119765. https://doi.org/10.1016/j.carbpol.2022.119765

Entezari A, Roohani I, Li G, Dunstan CR, Rognon P, Li Q, Jiang X, Zreiqat H (2019) Architectural design of 3D printed scaffolds controls the volume and functionality of newly formed bone. Adv Healthc Mater 8(1):e1801353. https://doi.org/10.1002/adhm.201801353

Feroz S, Dias G (2021) Hydroxypropylmethyl cellulose (HPMC) crosslinked keratin/hydroxyapatite (HA) scaffold fabrication, characterization and in vitro biocompatibility assessment as a bone graft for alveolar bone regeneration. Heliyon 7(11):e08294. https://doi.org/10.1016/j.heliyon.2021.e08294

Haugh MG, Murphy CM, O'Brien FJ (2010) Novel freeze–drying methods to produce a range of collagen-glycosaminoglycan scaffolds with tailored mean pore sizes. Tissue Eng Part C Methods 16(5):887–894. https://doi.org/10.1089/ten.TEC.2009.0422

Hayman EG, Pierschbacher MD, Suzuki S, Ruoslahti E (1985) Vitronectin: a major cell attachment-promoting protein in fetal bovine serum. Exp Cell Res 160(2):245–258. https://doi.org/10.1016/0014-4827(85)90173-9

He J, Genetos DC, Yellowley CE, Leach JK (2010) Oxygen tension differentially influences osteogenic differentiation of human adipose stem cells in 2D and 3D cultures. J Cell Biochem 110(1):87–96. https://doi.org/10.1002/jcb.22514

He X, Fan X, Feng W, Chen Y, Guo T, Wang F, Liu J, Tang K (2018) Incorporation of microfibrillated cellulose into collagen–hydroxyapatite scaffold for bone tissue engineering. Int J Biol Macromol 115:385–392. https://doi.org/10.1016/j.ijbiomac.2018.04.085

Hokmabad VR, Davaran S, Aghazadeh M, Rahbarghazi R, Salehi R, Ramazani A (2019) Fabrication and characterization of novel ethyl cellulose-grafted-poly (varepsilon-caprolactone)/alginate nanofibrous/macroporous scaffolds incorporated with nano-hydroxyapatite for bone tissue engineering. J Biomater Appl 33(8):1128–1144. https://doi.org/10.1177/0885328218822641

Huang Z, Nelson ER, Smith RL, Goodman SB (2007) The sequential expression profiles of growth factors from osteoprogenitors [correction of osteroprogenitors] to osteoblasts in vitro. Tissue Eng 13(9):2311–2320. https://doi.org/10.1089/ten.2006.0423

Huri PY, Ozilgen BA, Hutton DL, Grayson WL (2014) Scaffold pore size modulates in vitro osteogenesis of human adipose-derived stem/stromal cells. Biomed Mater 9(4):045003. https://doi.org/10.1088/1748-6041/9/4/045003

Hutmacher DW, Schantz JT, Lam CX, Tan KC, Lim TC (2007) State of the art and future directions of scaffold-based bone engineering from a biomaterials perspective. J Tissue Eng Regen Med 1(4):245–260. https://doi.org/10.1002/term.24

Karageorgiou V, Kaplan D (2005) Porosity of 3D biomaterial scaffolds and osteogenesis. Biomaterials 26(27):5474–5491. https://doi.org/10.1016/j.biomaterials.2005.02.002

Kilpadi KL, Chang P-L, Bellis SL (2001) Hydroxylapatite binds more serum proteins, purified integrins, and osteoblast precursor cells than titanium or steel. J Biomed Mater Res 57(2):258–267. https://doi.org/10.1002/1097-4636(200111)57:2%3c258::Aid-jbm1166%3e3.0.Co;2-r

Kim HW, Knowles JC, Kim HE (2005) Hydroxyapatite and gelatin composite foams processed via novel freeze–drying and crosslinking for use as temporary hard tissue scaffolds. J Biomed Mater Res A 72(2):136–145. https://doi.org/10.1002/jbm.a.30168

Lee DY, Lee SY, Yun SH, Jeong JW, Kim JH, Kim HW, Choi JS, Kim GD, Joo ST, Choi I, Hur SJ (2022) Review of the current research on fetal bovine serum and the development of cultured meat. Food Sci Anim Resour 42(5):775–799. https://doi.org/10.5851/kosfa.2022.e46

Lian JB, Stein GS (1995) Development of the osteoblast phenotype: molecular mechanisms mediating osteoblast growth and differentiation. Iowa Orthop J 15:118–140

Lin N, Dufresne A (2014) Nanocellulose in biomedicine: current status and future prospect. Eur Polymer J 59:302–325. https://doi.org/10.1016/j.eurpolymj.2014.07.025

Livak KJ, Schmittgen TD (2001) Analysis of relative gene expression data using real-time quantitative PCR and the 2− ΔΔCT method. Methods 25(4):402–408. https://doi.org/10.1006/meth.2001.1262

Masruchin N, Park B-D, Causin V, Um IC (2015) Characteristics of TEMPO-oxidized cellulose fibril-based hydrogels induced by cationic ions and their properties. Cellulose 22(3):1993–2010. https://doi.org/10.1007/s10570-015-0624-0

McClary KB, Ugarova T, Grainger DW (2000) Modulating fibroblast adhesion, spreading, and proliferation using self-assembled monolayer films of alkylthiolates on gold. J Biomed Mater Res 50(3):428–439. https://doi.org/10.1002/(sici)1097-4636(20000605)50:3%3c428::Aid-jbm18%3e3.0.Co;2-h

Murphy CM, Haugh MG, O'Brien FJ (2010) The effect of mean pore size on cell attachment, proliferation and migration in collagen–glycosaminoglycan scaffolds for bone tissue engineering. Biomaterials 31(3):461–466. https://doi.org/10.1016/j.biomaterials.2009.09.063

Murshed M, McKee MD (2010) Molecular determinants of extracellular matrix mineralization in bone and blood vessels. Curr Opin Nephrol Hypertens 19(4):359–365. https://doi.org/10.1097/MNH.0b013e3283393a2b

Mygind T, Stiehler M, Baatrup A, Li H, Zou X, Flyvbjerg A, Kassem M, Bunger C (2007) Mesenchymal stem cell ingrowth and differentiation on coralline hydroxyapatite scaffolds. Biomaterials 28(6):1036–1047. https://doi.org/10.1016/j.biomaterials.2006.10.003

Ojansivu M, Rashad A, Ahlinder A, Massera J, Mishra A, Syverud K, Finne-Wistrand A, Miettinen S, Mustafa K (2019) Wood-based nanocellulose and bioactive glass modified gelatin-alginate bioinks for 3D bioprinting of bone cells. Biofabrication 11(3):035010. https://doi.org/10.1088/1758-5090/ab0692

Oryan A, Alidadi S, Moshiri A, Maffulli N (2014) Bone regenerative medicine: classic options, novel strategies, and future directions. J Orthop Surg Res 9(1):18. https://doi.org/10.1186/1749-799X-9-18

Palaveniene A, Tamburaci S, Kimna C, Glambaite K, Baniukaitiene O, Tihminlioglu F, Liesiene J (2019) Osteoconductive 3D porous composite scaffold from regenerated cellulose and cuttlebone-derived hydroxyapatite. J Biomater Appl 33(6):876–890. https://doi.org/10.1177/0885328218811040

Petrauskaite O, Juodzbalys G, Viskelis P, Liesiene J (2016) Control of the porous structure of cellulose-based tissue engineering Scaffolds by means of lyophilization. Cellul Chem Technol 50(1):23–30

Price PA, Toroian D, Chan WS (2009) Tissue-nonspecific alkaline phosphatase is required for the calcification of collagen in serum: a possible mechanism for biomineralization. J Biol Chem 284(7):4594–4604. https://doi.org/10.1074/jbc.M803205200

Rashad A, Mustafa K, Heggset EB, Syverud K (2017) Cytocompatibility of wood-derived cellulose nanofibril hydrogels with different surface chemistry. Biomacromol 18(4):1238–1248. https://doi.org/10.1021/acs.biomac.6b01911

Rashad A, Mohamed-Ahmed S, Ojansivu M, Berstad K, Yassin MA, Kivijarvi T, Heggset EB, Syverud K, Mustafa K (2018) Coating 3D printed polycaprolactone scaffolds with nanocellulose promotes growth and differentiation of mesenchymal stem cells. Biomacromol 19(11):4307–4319. https://doi.org/10.1021/acs.biomac.8b01194

Ratheesh G, Shi M, Lau P, Xiao Y, Vaquette C (2021) Effect of dual pore size architecture on in vitro osteogenic differentiation in additively manufactured hierarchical scaffolds. ACS Biomater Sci Eng 7(6):2615–2626. https://doi.org/10.1021/acsbiomaterials.0c01719

Saito T, Okita Y, Nge TT, Sugiyama J, Isogai A (2006) TEMPO-mediated oxidation of native cellulose: microscopic analysis of fibrous fractions in the oxidized products. Carbohydr Polym 65(4):435–440. https://doi.org/10.1016/j.carbpol.2006.01.034

Sicchieri LG, Crippa GE, de Oliveira PT, Beloti MM, Rosa AL (2012) Pore size regulates cell and tissue interactions with PLGA-CaP scaffolds used for bone engineering. J Tissue Eng Regen Med 6(2):155–162. https://doi.org/10.1002/term.422

Sofi HS, Akram T, Shabir N, Vasita R, Jadhav AH, Sheikh FA (2021) Regenerated cellulose nanofibers from cellulose acetate: incorporating hydroxyapatite (HAp) and silver (ag) nanoparticles (NPs), as a scaffold for tissue engineering applications. Mater Sci Eng C Mater Biol Appl 118:111547. https://doi.org/10.1016/j.msec.2020.111547

Soni B, Hassan el B, Mahmoud B (2015) Chemical isolation and characterization of different cellulose nanofibers from cotton stalks. Carbohydr Polym 134:581–589. https://doi.org/10.1016/j.carbpol.2015.08.031

Syverud K, Pettersen SR, Draget K, Chinga-Carrasco G (2014) Controlling the elastic modulus of cellulose nanofibril hydrogels—scaffolds with potential in tissue engineering. Cellulose 22(1):473–481. https://doi.org/10.1007/s10570-014-0470-5

Tang D, Tare RS, Yang LY, Williams DF, Ou KL, Oreffo RO (2016) Biofabrication of bone tissue: approaches, challenges and translation for bone regeneration. Biomaterials 83:363–382. https://doi.org/10.1016/j.biomaterials.2016.01.024

Thavornyutikarn B, Chantarapanich N, Sitthiseripratip K, Thouas GA, Chen Q (2014) Bone tissue engineering scaffolding: computer-aided scaffolding techniques. Prog Biomater 3:61–102. https://doi.org/10.1007/s40204-014-0026-7

Tsuruga E, Takita H, Itoh H, Wakisaka Y, Kuboki Y (1997) Pore size of porous hydroxyapatite as the cell-substratum controls BMP-induced osteogenesis. J BioChem 121(2):317–324

Vimalraj S, Arumugam B, Miranda PJ, Selvamurugan N (2015) Runx2: structure, function, and phosphorylation in osteoblast differentiation. Int J Biol Macromol 78:202–208. https://doi.org/10.1016/j.ijbiomac.2015.04.008

Webster TJ, Schadler LS, Siegel RW, Bizios R (2001) Mechanisms of enhanced osteoblast adhesion on nanophase alumina involve vitronectin. Tissue Eng 7(3):291–301. https://doi.org/10.1089/10763270152044152

Whang K, Healy KE, Elenz DR, Nam EK, Tsai DC, Thomas CH, Nuber GW, Glorieux FH, Travers R, Sprague SM (1999) Engineering bone regeneration with bioabsorbable scaffolds with novel microarchitecture. Tissue Eng 5(1):35–51. https://doi.org/10.1089/ten.1999.5.35

Wilson CJ, Clegg RE, Leavesley DI, Pearcy MJ (2005) Mediation of biomaterial-cell interactions by adsorbed proteins: a review. Tissue Eng 11(1–2):1–18. https://doi.org/10.1089/ten.2005.11.1

Xavier JR, Thakur T, Desai P, Jaiswal MK, Sears N, Cosgriff-Hernandez E, Kaunas R, Gaharwar AK (2015) Bioactive nanoengineered hydrogels for bone tissue engineering: a growth-factor-free approach. ACS Nano 9(3):3109–3118. https://doi.org/10.1021/nn507488s

Yang D, Lu X, Hong Y, Xi T, Zhang D (2013) The molecular mechanism of mediation of adsorbed serum proteins to endothelial cells adhesion and growth on biomaterials. Biomaterials 34(23):5747–5758. https://doi.org/10.1016/j.biomaterials.2013.04.028

Zhu X, Chen J, Scheideler L, Altebaeumer T, Geis-Gerstorfer J, Kern D (2004) Cellular reactions of osteoblasts to micron- and submicron-scale porous structures of titanium surfaces. Cells Tissues Organs 178(1):13–22. https://doi.org/10.1159/000081089